Optimization and characterization of a flow cell for heat-transfer-based biosensing

Phys. Status Solidi A **214,** No. 9, 1600758 (2017) / **DOI** 10.1002/pssa.201600758

physica status solidi a
www.pss-a.com
applications and materials science

Part of Topical Section on
Engineering of Functional Interfaces

Optimization and characterization of a flow cell for heat-transfer-based biosensing

Wouter Stilman[**,1], **Stijn Jooken**[**,2], **Gideon Wackers**[1], **Peter Cornelis**[1], **Mehran Khorshid**[1], **Derick Yongabi**[1], **Onno Akkermans**[3], **Simba Dyson**[3], **Bart van Grinsven**[3], **Thomas Cleij**[3], **Leo van Ijzendoorn**[2], **Patrick Wagner**[1], **and Kasper Eersels**[*,1]

[1] Soft-Matter Physics and Biophysics Section, KULeuven, Celestijnenlaan 200 D, B-3001 Leuven, Belgium
[2] Department of Applied Physics, Technische Universiteit Eindhoven, PO Box 513, Eindhoven, The Netherlands
[3] Maastricht Science Programme, Maastricht University, PO Box 616, Maastricht, The Netherlands

Received 20 October 2016, revised 21 December 2016, accepted 23 January 2017
Published online 20 February 2017

Keywords bacteria, biosensors, COMSOL simulations, heat transfer, interfaces, thermal resistance

[*] Corresponding author: e-mail kasper.eersels@kuleuven.be, Phone: +3216327842, Fax: +3216327984
[**] Both authors contributed equally to this work.

In this article, we report on the development of a flow cell optimized for the heat-transfer method, a versatile biosensing technique. The design of the flow cell ensures that the heat flow is focused with minimal heat loss through the surroundings of the cell. This results in a more stable measuring signal and an improved sensitivity of the measuring technique. The sensor was characterized by performing background measurements in air, water, and phosphate buffered saline (PBS) solution. Heat flow through the setup was simulated using COMSOL in order to provide insight in the contribution of convection to the heat flow and recommendations for possible future improvements to the cell. Additionally, a two-step algorithm for calculating thermal resistance was defined, allowing the user to accurately derive thermal conductivity from experimental data. Finally, the potential of the flow cell for bacteria (*Escherichia coli*) detection was assessed and compared with the results obtained in the original HTM setup in a similar experiment. This experiment demonstrates that we were able to improve the limit-of-detection (LoD) to 2.10×10^4 colony forming units (CFU) mL^{-1} by changing the geometry of the measuring cell.

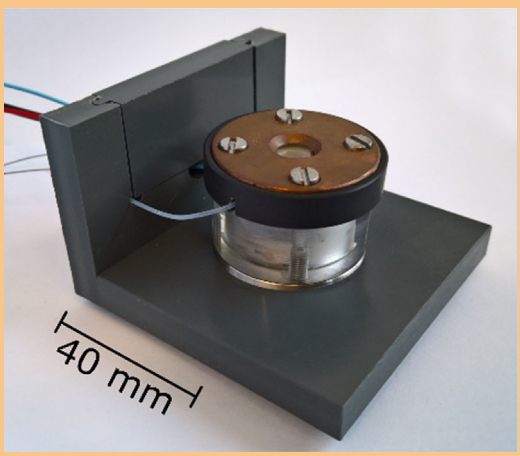

Sensor setup for thermal biodetection experiments with a directed heat flow.

1 Introduction Over the past few decades, multiple biosensors have been developed for application in diverse fields including medical diagnostics, toxicology, and environmental analysis [1, 2]. As biological receptors are difficult to incorporate into commercial devices, biomimetic sensors, which use synthetic receptors, are emerging as an alternative to detect the analyte of interest [3–5]. In case of the detection of macromolecular entities such as proteins, mammalian cells or pathogens, surface-imprinted polymers (SIPs) have been particularly used as synthetic receptors in these sensing platforms [6–8]. Biological and synthetic receptors have been combined with electrochemical [9, 10], optical [11, 12], microgravimetrical [13, 14], and thermal [15] transducers for the development of a wide range of applications.

Recently, a novel thermal transducer principle, coined the heat-transfer method (HTM), has been developed by the authors of this article. This fast, label-free, and sensitive platform has proven to be very versatile in terms of biosensing [16]. HTM is based on the analysis of thermal transport across a functionalized interface. To this extent, the temperature underneath the sample is kept constant by a temperature control unit consisting of a thermocouple, a heat source and a thermostat. The temperature above the solid–liquid interface is monitored over time. This enables the user to calculate the thermal resistance of the solid–liquid interface at any point in time. Changes occurring at the interface will alter its thermal resistance, which can be detected by the setup. HTM has been used for a wide range of applications including DNA mutation analysis [17], small molecule detection [18], and the detection of proteins [19], mammalian cells [20–22] and bacteria [23].

Although HTM has been combined successfully with numerous receptors for the applications summarized above, the sensitivity of the device is still a limitation when aiming at commercial applications for cell-based point-of-care diagnostics. It can be noted that the current limit of detection (LoD) might suffice to diagnose patients with a disease that is associated with a high count of disease-related cells in blood samples, such as chronic lymphocyte leukemia (CLL) [24]. Most cancers, however, are characterized by a much lower number of circulating tumor cells (CTCs) in patient blood samples. For example, breast cancer, concentrations of 1 tumor cell per mL blood and higher are considered a relevant marker for metastasis [25]. Likewise, while the concentration of the bacterium *Campylobacter jejuni* in fecal matter obtained from infected chickens might be as high as 10^8–10^{10} colony forming units per gram [26], the presence of bacteria in a drinking water sample is not tolerated [27]. For this application, the sensor should, therefore, be able to detect a single bacterial entity in a 100 mL sample.

In order to improve the sensitivity of the HTM methodology, this article introduces an optimized flow cell for thermal sensing. In the original design, a large copper heat sink was coupled to a Perspex flow cell to transfer heat to the functional interface. This way, the flow cell suffered from considerable heat loss to the environment and perturbations in the ambient temperature led to an extensive level of noise on the signal [17–23]. The new design should provide an improved focus of the heat flow through the functional interface, less heat loss through the cell surroundings, lower power consumption, and an improved temperature control within the heat provider. In addition, the temperature inside the flow cell is monitored much closer to the sensor surface, ensuring that the relative contribution of the functional interface to the overall thermal resistance increases. The accuracy of the optimized setup was studied by measuring the thermal resistance of water, air, and phosphate buffered saline (PBS) solution, and comparing the obtained values to theoretical values in the literature. In addition, the performance of the setup was optimized by tuning the proportional-integral-derivative (PID) parameters of the temperature control unit, in order to achieve a maximal sensitivity for cell detection at 37 °C. In addition, the heat transport inside the flow cell was simulated using COMSOL Multiphysics. In this way, the results obtained using the setup can be better understood and recommendations for further optimization of the design in the future can be given. Finally, the optimized HTM setup was tested by coating an aluminum chip with a SIP, imprinted with *Escherichia coli*. The performance of the optimized platform in a quantitative *E. coli* detection experiment was compared with the results obtained in an analogous experiment using the original flow cell, optimized for impedance spectroscopy but without stringent heat flow engineering [17].

2 Materials and methods

2.1 Optimized HTM setup and measuring scheme Following the system requirements defined in the introduction, a flow cell was designed, as schematically shown in Figure 1.

Aluminum chips ($10 \times 10 \times 1\,mm^3$, Brico N.V., Leuven, Belgium) were heated by a power resistor (Farnell, Grâce-Hollogne, Belgium) via a copper heat provider that has dimensions similar to the chip to minimize heat loss through the environment. The temperature of the copper (T_1) was measured by a thermocouple (type K, diameter 0.5 mm, TC Direct, Nederweert, the Netherlands). The signal is registered by a TC-08 thermocouple data logger (Picotech, United Kingdom) and transferred to a Labview-based program (National Instruments, Zaventem, Belgium). The software-based PID controller uses this information to adjust the voltage over the power resistor in order to keep T_1 constant at 37 °C. A liquid flow cell, with an inner volume of 160 μL, was made in polyether ether ketone (PEEK) and shielded by two O-rings defining a contact area of 36 mm^2

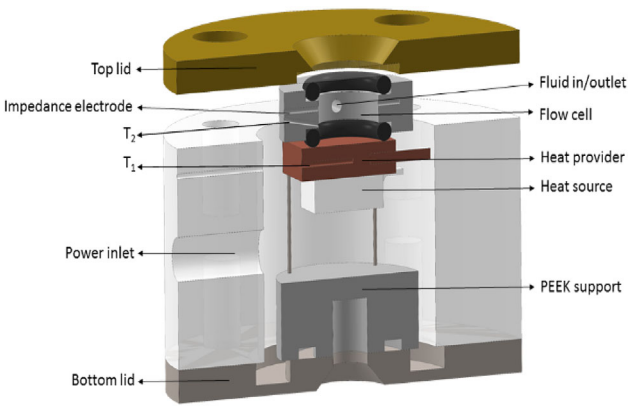

Figure 1 Schematic representation of the optimized HTM setup. The aluminum sensor chip is inserted between the heat provider and the flow cell. The heat flow is focused through the solid–liquid interface and monitored by two thermocouples, measuring the temperature of the heat provider (T_1) and the flow cell (T_2), measured at 1 mm above the chip surface) over time.

between the chip and the liquid. Given the height of 4.4 mm and a diameter of 6.8 mm, the aspect ratio Γ of the flow cell is 0.65. PEEK was chosen in function of its unique material properties allowing for disinfection with numerous solvents and autoclaving. The temperature of the flow cell containing the target cell solution (T_2) was monitored over time by a second thermocouple at 0.1 mm from the chip surface to minimize the amount of heat loss through the fluid column. By monitoring T_2 over time at a constant T_1, the heat-transfer resistance (R_{th}) at the solid–liquid interface can be derived at any point in time, using the equation: $R_{th} = (T_1 - T_2)/P$, with P being the power necessary to keep T_1 constant. Within this formula, it is assumed that all of the input power will flow through the functional interface.

Based on previous results with a similar PID optimization study on the original HTM setup [28], it was decided to sweep the P and I values between 1 and 12 in the current study with a step width of 1. The average thermal resistance was calculated at 37 °C in de-ionized water over a period of 30 min for each combination and the standard error (σ) was analyzed. In addition, the D value was fine-tuned in a similar manner, sweeping it from 0.1 to 1 with a step width of 0.1. All measurements performed using a blank aluminum chip and were repeated at least three times to obtain a standard deviation.

To assess the potential of the setup for accurately determining the thermal resistance, calibration measurements were performed in water, PBS, and air. For each of the calibration measurements, the temperature was increased stepwise from 25 over 30, 37, 40, 45, 50, 55, 60 to 65 °C. At each temperature, the signal was allowed to stabilize for 50 min and the average thermal resistance and error over this plateau were calculated. The experimentally obtained value for water was compared with the literature data.

In a final set of HTM measurements, the optimized setup and PID settings were used in a dose-response experiment. The liquid compartment was filled with PBS at the start of the experiment and the thermal resistance was allowed to stabilize for 30 min. Next, bacteria were introduced into the system (3 mL *E. coli* in PBS) at a flow rate of 2.5 mL min^{-1}, after which the thermal resistance was allowed to stabilize again for 30 min under stopped flow conditions for a faithful calibration of the measurement; the actual response time is only 5–10 min. Subsequently, the system was flushed two times consecutively. The cells were killed in the first step by flushing the setup with 70% ethanol, making them susceptible to removal by shear force in a second flushing step with PBS. Both rinsing steps were performed at a flow rate of 2.5 mL min^{-1}. The thermal resistance was left to stabilize for 30 min after both flushing steps. The chip was gradually exposed to a higher concentration of target cells, in order to construct a dose-response curve. Since previous work has demonstrated that the dynamic range of the device is located between 5×10^4 and 1×10^6 cells mL^{-1} [23], concentrations of 1, 2, 5, 10, 50, and 100×10^5 colony forming units (CFU) mL^{-1} were used. The LoD was defined as the concentration at which the signal corresponds to three times the largest standard error on the data. The obtained value was compared to the LoD obtained in an analogous experiment, using the previous setup described in Ref. [22].

2.2 Simulation study The HTM setup was analyzed by means of numerical simulations in COMSOL Multiphysics (COMSOL, Inc., Burlington, USA). Also, the contribution of buoyant convection to the heat transfer within the setup was studied and the effect of the dimension of the flow cell on this phenomenon was examined. A 3D stationary simulation study aims at providing insight to the time-independent advective contribution to the heat transport and the influence of the flow cell dimensions on this phenomenon and, therefore, the sensitivity of the device. This might lead to recommendations for further improvements to the flow cell. Additionally, a simulation was combined with experimental HTM data from calibration measurements in water and air, to verify whether the experimentally obtained results are comparable to reference values, such as the thermal conductivity κ of water. To be able to faithfully simulate the conditions within the setup, a 3D schematic representation of the setup in Fig. 1 was redrawn in COMSOL which is illustrated in Fig. 2, and the simulated materials and their characteristics can be found in Table 1.

The temperature of the copper heat provider (domain 1 in Fig. 2) was constraint to 37 °C and covered by the aluminum chip. The height of the flow cell (domain 10) is parametrically swept by varying the aspect ratio for a constant base radius. A thermocouple was inserted at 1 mm from the chip surface, while a gold wire, inserted into the setup for impedance measurements was placed at 1.5 mm above the chip surface. The PEEK flow cell was surrounded by a PVC collar for sample positioning, while the PEEK support was embedded in a Perspex shell. The copper top lid has a glass window topping of the flow cell for visual inspection for air bubbles and microscopic observations of

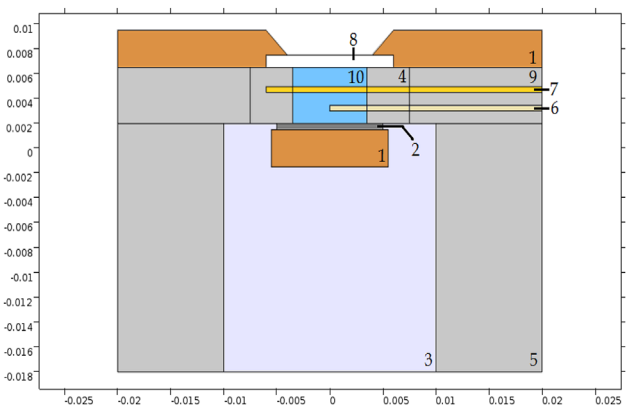

Figure 2 Cross-section of the geometry of the 3D model of the HTM setup as implemented in COMSOL Multiphysics. The units of both axes are expressed in meters.

Table 1 Materials used in the COMSOL model in Figure 2, including their most relevant thermal properties (heat capacity at constant pressure C_p, density ρ, thermal conductivity κ).

nr.	material	C_p (J/kg K)	ρ (kg m^{-3})	κ (W/m K)
1	copper	385	8700	400
2	aluminum	900	2700	238
3	air	1000	1.12	0.027
4	PEEK	1700	1320	0.25
5	perspex	1466	1190	0.18
6	stainless steel	445	8900	90.7
7	gold	129	19300	317
8	glass	703	2203	1.38
9	PVC	1000	1760	0.1
10	water	4186	1000	0.62

the functional interface. An image of the fully assembled device can be found in the abstract figure.

In domains 1–9, the heat transport was modeled via Fourier's law

$$\kappa \nabla^2 T = 0, \tag{1}$$

where κ represents the thermal conductivity in (W/m K) and T the temperature in K. Within the flow cell (domain 10) the simultaneous presence of a density gradient ($d\rho/dz < 0$), produced by the temperature gradient, and a gravitational body force $-|F_z|\hat{z}$ gives rise to an advective contribution to the heat transport, determined in size and appearance by the Rayleigh number (Eq. 2).

$$\frac{g\beta(T_1 - T_2)L^3}{\alpha v} = 0, \tag{2}$$

where g is the gravitational constant in N kg^{-1}, β the thermal expansion coefficient in K^{-1}, $(T_1 - T_2)$ the temperature difference between bottom and top of the fluid cell, l the distance between bottom and top in m, α the thermal diffusivity in m^2 s^{-1}, and v the kinematic viscosity in Pa · s. In addition to an energy balance (Eq. 3), the governing set of equations now consists of a momentum balance (Eq. 4) and a mass balance (Eq. 5).

$$\rho C_p \boldsymbol{u} \cdot \nabla T - k\nabla^2 T = 0, \tag{3}$$

$$(\boldsymbol{u} \cdot \nabla)\boldsymbol{u} = \nabla \cdot \left[-pI + v\left(\nabla \boldsymbol{u} + (\nabla \boldsymbol{u})^T\right) - \frac{2}{3}v(\nabla \cdot \boldsymbol{u})I\right] + \boldsymbol{g}, \tag{4}$$

$$\nabla \cdot (\rho \boldsymbol{u}) = 0, \tag{5}$$

where $\boldsymbol{u}$ denotes the velocity field in m s^{-1}, p the pressure in Pa, C_p the heat capacity at constant pressure in J/kg K, ρ the density in kg m^{-3}, and I the unity tensor.

These equations are fully coupled using the non-isothermal laminar flow interface. The choice for a laminar flow model is justified because the temperature difference between bottom and top ($T_{ext} = 22\,^{\circ}$C) of the cylindrical domain cannot exceed 15 °C, which results in a Rayleigh number well below the critical number for the onset of turbulent convection.

As boundary conditions, cooling by free external convection in air is set for the top and sides of the geometry by defining an outward heat flux (6) proportional to the temperature difference with its surroundings and a heat transfer coefficient h for horizontal and vertical-heated plates.

$$-\hat{n}\boldsymbol{q} = h(T_{ext} - T), \tag{6}$$

where $\hat{n}$ is the surface normal and q the heat flux in W m^{-2}. The mesh convergence was studied over three different mesh sizes. Convergence criteria were a constant temperature in the center at the top side of the flow cell and a minimal influence on the isotherms. As a result of this study, 0.3 mm sized tetrahedral elements were chosen in the fluid domain. This yields results suitable for qualitative interpretation within a reasonable amount of time. The nonlinear problem is solved in a fully coupled approach using an iterative GMRES solver.

2.3 Bacterial culture *E. coli* (ATCC® 8739™) strains were obtained from DSMZ (Deutsche Sammlung von Mikroorganismen und Zellkulturen, Braunschweig, Germany). To this extent, 20 ml nutrient broth (NB, ×929.1 ROTH) was inoculated with a single colony of *E. coli* and allowed to grow overnight at 37 °C while shaking. Prior to imprinting, 1 ml of the overnight culture was diluted in 20 ml of the broth, and allowed to grow at 37 °C for 3 h or until an optical density of 1 was obtained at 600 nm (8×10^8 cells ml^{-1}). Afterwards, the cells were harvested by centrifugation and the pellets were washed one time with PBS, and resuspended in PBS to achieve the desired concentrations.

2.4 Surface imprinting procedure Polyurethane layers were formed by dissolving 122 mg of 4,4′-diisocyanatodiphenylmethane, 222 mg of bisphenol A and 25 mg of phloroglucinol in 500 µl of anhydrous tetrahydrofuran (THF). All reagents were used as received from Sigma–Aldrich N.V. (Diegem, Belgium) and had a purity of minimum 99.9%. This mixture was stirred at 65 °C for 200 min under an inert nitrogen atmosphere until the polymer solution reached its gelling point. Then, the solution was diluted in a 1:5 ratio in THF and spin coated for 60 s at 2000 rpm onto 1 cm^2 aluminum substrates. In parallel, polydimethylsiloxane (PDMS) stamps were covered with cells to stamp the cells into the spin-coated polyurethane layer. PDMS stamps were made using the Sylgard 184 silicone elastomer kit (Malvom N.V., Schelle, Belgium). Then, the *E. coli* suspension in PBS (400 µl) was

applied onto the PDMS stamp. After 20 min of sedimentation time, the excess fluid was removed by spin coating at 3000 rpm for 60 s to create a dense monolayer of cells on the stamp surface. The cell-covered stamp was gently pressed onto the polyurethane layer and cured for 18 h at 65 °C under nitrogen atmosphere. After curing, the stamp was removed from the surface and bound bacteria were removed by rinsing the layer with 70% ethanol and PBS, leaving behind selective binding cavities on the polyurethane surface [22].

3 Results and discussion

3.1 PID tuning The effect of the PID values on the noise on the signal were studied by a parametric sweep as described in Section 2.1. The average noise on the signal and its standard error were calculated for each P and I combination. The best combinations are summarized in Table 2. From the PID tuning it can be concluded that a broad range of P and I settings can be considered as optimal as the average noise on the signal observed using these settings does not significantly change. An additional tuning of the D parameter (not shown) did not significantly improve the noise levels on the signal. These findings are in line with similar PID tuning schemes, performed on the original HTM setup in previous work [28] and indicate that a full PID tuning might not be necessary when future modifications are made to the setup. Furthermore, it implies that the device can be used in various surroundings without significantly affecting its sensitivity.

3.2 Flow cell calibration The setup's behavior was characterized in different media at different temperatures. The temperature in the flow cell was measured at 0.1 mm from the surface. The results of these experiments indicate that the power consumption is a factor two lower in comparison to the original setup, indicating a more homogeneous flow through the flow cell. The thermal resistance data (shown in Fig. 3) indicate that the HTM device is able to measure thermal resistance in a very consistent manner over most of the temperature range. However, at low temperatures, we see that the results deviate as the ambient temperature (21 °C) influences the PID steering of T_1 to a large extent.

Table 2 Set of optimized PID settings. Measurements were performed in water at 37 °C on an aluminum chip. The average noise on the thermal resistance and a standard error (in $K W^{-1}$) were calculated and the settings with optimal noise levels are shown.

P	I	average noise ($K W^{-1}$)	standard error ($K W^{-1}$)
1	4	0.05	0.02
1	5	0.05	0.02
1	11	0.05	0.03
1	3	0.05	0.02
1	6	0.05	0.02
1	10	0.06	0.02
1	9	0.07	0.01
1	8	0.06	0.02
1	12	0.05	0.03
2	11	0.06	0.02

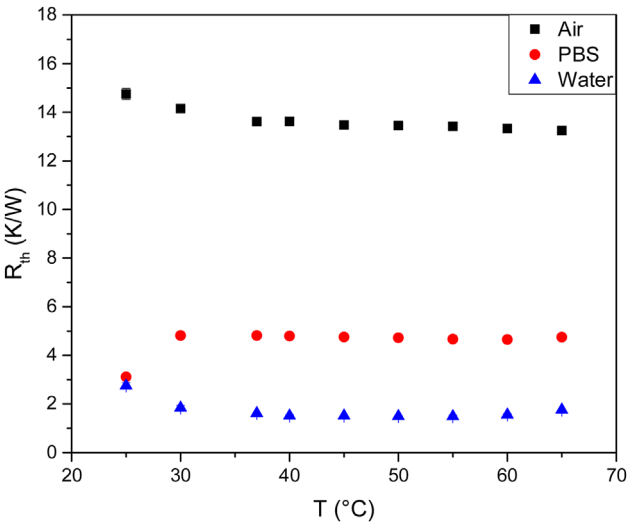

Figure 3 Calibration measurements at increasing temperatures in water (blue triangles), air (red dots), and PBS (black squares). The error bars are typically smaller than the symbol size.

When looking at the data in Fig. 3, it can be concluded that R_{th} values of 1.55 ± 0.12, 4.74 ± 0.09, and 13.54 ± 0.11 K W^{-1} were obtained at 37 °C for water, PBS, and air, respectively. These data demonstrate that the thermal conductivity of PBS will be lower than water but higher than air. This can be explained by the fact that water molecules will form a hydration shell around the ions, decreasing their mobility. Although these values might provide an estimate of the thermal resistance, which is sufficient for sensing purposes, an accurate estimation would obviously require a more thorough study and calculation. For instance, it can be noted that the experimentally obtained value for air is only 9 times higher than the value for water. However, when comparing the results to the literature values for the thermal conductivity of both water and air, a ratio of 23 would be expected [29, 30]. This can be partly explained by fact that the PEEK wall of the flow cell has a higher conductivity than air, resulting in heat loss through the walls of the setup. The heat flow through the sensor will therefore be examined in closer detail in the next sections.

3.3 Simulation of heat flow In order to model the temperature profile of the configuration shown in Fig. 1, the effect of buoyant convection, which was analyzed in COMSOL (Fig. 4), has to be taken into account. The flow cell, which has an aspect ratio (Γ, defined by the height/diameter ratio) of 0.65, does not fully comply with the theory of convection in cylindrical barrels, as the temperature of the top plate (copper lid plus 1 mm glass plate) of the setup is not actively controlled but cooled passively by ambient air through natural convection. The Rayleigh

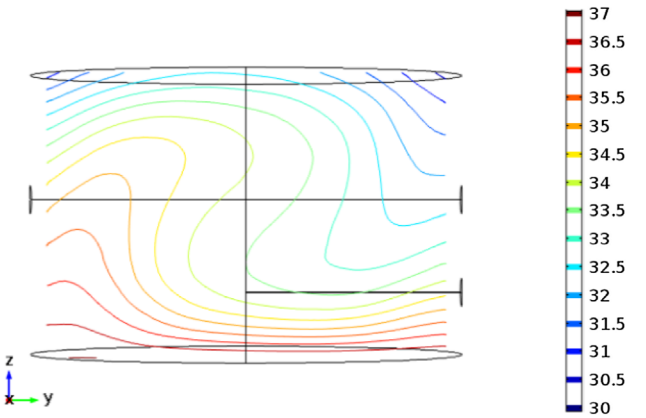

Figure 4 Isotherms (°C) at 1.5 mm off the vertical midplane of the flow cell illustrating the asymmetric flow pattern inside the setup at 37 °C. The thermocouple (lower horizontal line) and gold wire (upper horizontal line) are shown and clearly influence the flow inside the liquid compartment of the setup. To illustrate the concept in a clear manner, the thermocouple was put at 1 mm above the chip surface instead of 0.1 mm.

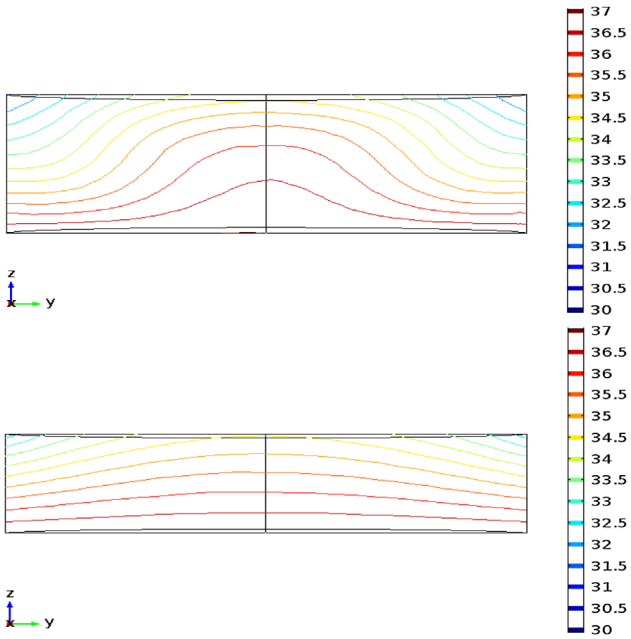

Figure 5 Isotherms (°C) in the vertical midplane of the flow cell at 37 °C for fictional aspect ratios 0.35 (top) and 0.25 (bottom).

number inside the cell can, therefore, be considered as ill-defined and position dependent. The top plate will serve as a heat sink but due to the glass plate directly on top of the liquid, the heat sink effect will be drawn to the sides, creating an asymmetric flow starting at 25 °C (onset of convection). Furthermore, the insertion of a gold wire (for electrochemical measurements such as impedance spectroscopy) and a thermocouple (for HTM purposes) further forces the convection into an asymmetric configuration, as can be seen in the COMSOL simulation in Fig. 4.

3.4 Suppression of convection To overcome convection it is possible to simply invert the setup and heat the cylindrical fluid column inside the flow cell from above which has been done for the detection of DNA mutations [17] and proteins [19]. However, for the detection of macromolecular targets such as cells or bacteria it is necessary to allow the target particles to sediment to the functional interface located on top of the copper heat provider. Therefore, inverting the setup is not an option in this case. Alternatively, it is possible to change the dimensions of the fluid cell to diminish convection inside the setup. The determining factor governing convection is the temperature difference $T_1 - T_2$ between the top and the bottom of the fluid cell. This difference can be influenced by adjusting the height of the flow cell, thereby decreasing the aspect ratio. Decreasing the aspect ratio by changing the diameter of the flow cell will not influence convection. Figure 5 illustrates the results obtained in a COMSOL simulation with fictional flow cells in which Γ has been decreased to 0.35 and 0.25, respectively. The simulations show that lowering the aspect ratio will result in a more homogeneous heat flow through the cell. However, due to the large copper heat sink and the glass window, the temperature difference will never be truly uniform.

To obtain more control over the temperature of the top lid, a fictional flow cell without a glass window in the top lid was used for simulations. The flow pattern in Fig. 6 demonstrates that by replacing the current top lid with a full copper cylinder with the same base radius as the container and a uniform height of 2 mm, a more homogeneous heat flow can be achieved. In this way, convection can be ruled out up to an aspect ratio of 0.3. Even at higher aspect ratios, convection is decreased significantly, as can be seen in the flow pattern in Fig. 6. However, copper can be detrimental for biological samples and might negatively affect impedance spectroscopy due to building up electrochemical voltages. Furthermore, the top lid needs to be optically transparent to verify that the flow cell is devoid of air bubbles. Therefore, synthetic sapphire could be a good

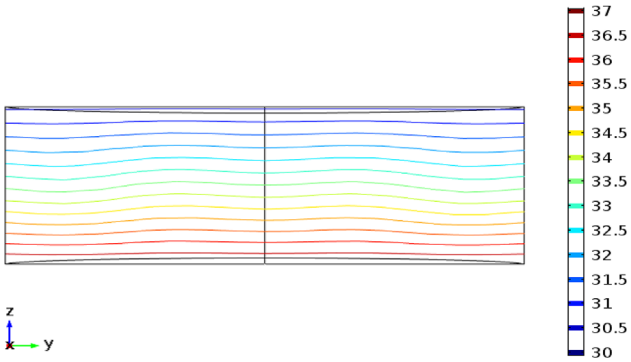

Figure 6 Isotherms (°C) in the vertical midplane of a flow cell (37 °C, $\Gamma = 0.35$) where the glass plate on top is removed and a solid copper lid is used.

alternative for the glass cover as it has a much higher thermal conductivity ($\kappa = 30.3$ W/m K) in comparison to glass ($\kappa = 1.38$ W/m K) [31].

3.5 Two-step thermal resistance calibration The thermal resistance values obtained in Section 3.2 are only approximations because an unknown fraction of the heating power is dissipated to the ambient without actually passing through the solid–liquid interface. Theoretically, in the absence of convection, the thermal resistance for a cylinder can be calculated from the following formula, with h and A being the height and surface area of the cylinder, respectively:

$$R_{\text{th}} = \frac{1}{k}\frac{h}{A}. \tag{7}$$

Given the diameter of the flow cell and the fact that the thermocouple was placed at 0.10 ± 0.02 mm of the chip surface to avoid convection and to minimize the heat loss through the fluid column inside the flow cell, it is possible to determine the theoretical thermal resistance by using the literature value for κ_{water} (0.624 W/m K), this would result in 4.23 K/W for water. Although the experimentally obtained value (1.55 K W^{-1}) is still in the same order of magnitude, there is a significant difference. This can be attributed to the fact that the above used R_{th}-formula $(T_1 - T_2)/P$ is not sufficiently accurate to determine the exact thermal resistance value. For instance, the formula takes into account the power necessary to keep T_1 constant, while this is not the amount of heat flowing through the chip, and the flow cell as part of the heat will dissipate through the side walls and the bottom of the setup. Therefore, the experimentally obtained value will be an underestimation of the true value.

As the absolute heat flux through the sensitive area of the chip was not known, the formula for the thermal resistance was revisited based on the assumption that the environment of the sensor is identical for a measurement in air and water. To get a good estimate of the heat loss through the environment (defined as P_{d}, the power dissipated to the ambient), a reference measurement in air is performed as schematically illustrated in Fig. 7. From the data obtained in this experiment, it is possible to calculate the fraction of power passing through the air column inside the cell (P_{a}) according to following formula:

$$P_{\text{a}} = \frac{\Delta T_{\text{air}}}{R_{\text{th}}} = \Delta T_{\text{air}} \cdot \frac{\kappa_{\text{air}} \cdot A}{h}. \tag{8}$$

From the experiments shown in Fig. 3, a value for ΔT_{air} of 3.55 ± 0.04 K can be obtained. Inserting the dimensions of the cell and the literature value for κ_{air} of 0.0262 W/m · K in Eq. (2), yielded a P_{a} of 33.8 ± 8.2 mW. By subtracting P_{a} from the total power provided by the resistor at 37 °C ($P_{\text{total}} = 260.3 \pm 2.9$ mW) a value of 226.5 ± 11.2 mW was obtained for P_{d}.

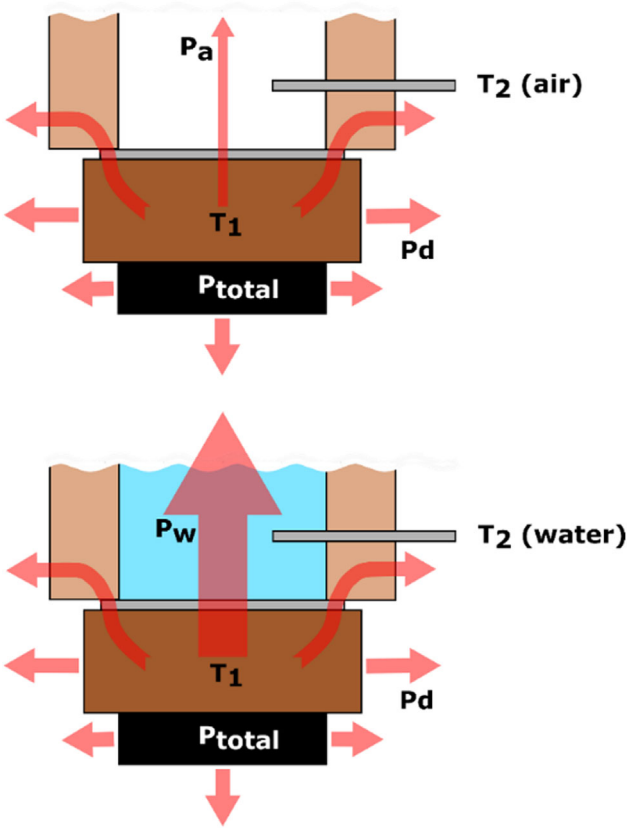

Figure 7 Illustration of the heat flow in the flow cell when filled with air (top) and water (bottom). As the power lost through the ambient, P_{d}, is approximately equal in both conditions, the difference between the power input approximates the heat flow through the water column.

These data were used to correct the experimentally obtained data from a calibration measurement in water, summarized in Fig. 3. As P_{d} was hypothesized to be equal for a measurement in both water and air, the amount of power flowing through the water filled column (P_{w}) equals the total power provided by the power resistor at 37 °C ($P_{\text{total}} = 332.3 \pm 0.003$ mW) minus P_{d}, obtained from the reference measurement in air, yielding a value of 105.8 ± 11.1 W for P_{w}. The thermal resistance of the flow cell in water can therefore be calculated from following equation:

$$R_{\text{th water}} = \frac{\Delta T_{\text{water}}}{P_{\text{w}}}. \tag{9}$$

Filling in the experimental data for ΔT_{water} (0.540 ± 0.001 K) in Eq. (3), yielded an $R_{\text{th water}}$ of 5.1 ± 0.54 K W^{-1}. Using Eq. (1) and the dimensions of the cell, this would result in a κ_{water} of 0.54 ± 0.18 W/m K, corresponding well with the theoretical value of 0.624 W/m K at 37 °C [29]. However, it has to be noted that the error in the corrected value is still relatively large

due to the uncertainty on the distance between the thermocouple and the chip surface.

3.6 Sensitivity test To assess whether the improved geometry of the flow cell has led to a significant improvement of the sensitivity of the methodology in biosensing applications, the optimized setup was tested in a quantitative binding assay for *E. coli* on SIP-covered aluminum chips. In parallel, the same experiment was performed using the original flow cell. The results of these experiments indicate that for both the original flow cell described in Refs. [22, 23] and the flow cell developed in this study, the sensor responds in linear fashion to concentrations between 10^4 and 10^5 CFU mL^{-1} after which the signal saturates (Fig. 8). However, the change in R_{th}-signal in response to an increasing concentration of target cells, appears to be bigger for the new setup over the entire concentration range. In addition, the noise on the signal is considerably smaller for the experiment on the new flow cell. In order to estimate the net effect on the sensitivity of the setup, the data were fitted exponentially ($R_{th} = a_1 + a_1 * \exp(-c/a_3)$) and the LoD was defined as three times the maximal error on the thermal resistance signal (3σ method). The intercept of this 3σ and the linear part of the exponential fit yielded a theoretical LoD of 2.10 and 4.65×10^4 CFU mL^{-1} for the optimized and original flow cell, respectively. From these findings it can be concluded that optimizing the design of the flow cell has improved the sensitivity of the methodology by approximately a factor two. This is a good starting point for further lowering the detection limit. The repeated exposure strategy, previously introduced by the authors, is a promising approach in this respect [21, 23]. Within this method, the receptor layer is repeatedly exposed to the sample under study. The signal gradually increases with each exposure cycle until it reaches the value corresponding to 3σ.

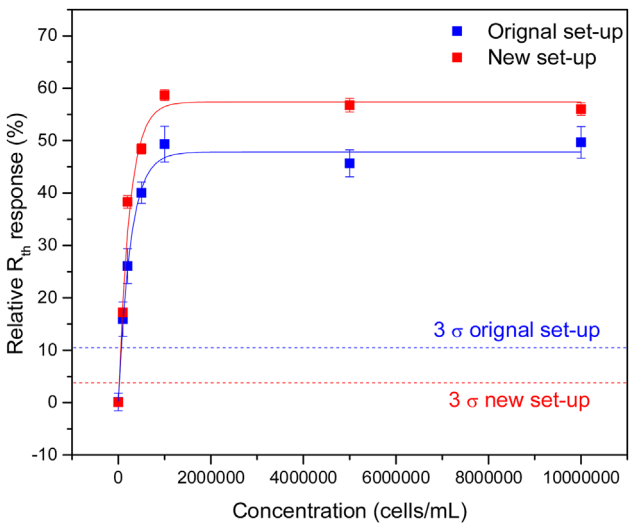

Figure 8 Dose-response curve exposing a SIP-covered aluminum chip to *E. coli* in PBS at concentrations of 0, 1, 2, 5, 10, 50, and 100×10^5 CFU mL^{-1}. The results indicate that the improved flow cell (red curve) is superior over the original flow cell (blue). The solid lines indicate an exponential fit over the data ($R^2 = 0.99$ in both cases), while the dashed line represents the limit-of-detection level, defined as three times the maximal error on the data (3σ).

4 Conclusions The results of the study presented in this article demonstrate that it is not necessary to perform an entire PID tuning scheme for HTM whenever adjustments are made to the flow cell design or when measuring at different temperatures. The result of the PID tuning experiment indicates that an optimal PID setting does not exist, but a range of settings can be applied to achieve an optimal noise level on the thermal resistance signal while still maintaining a stringent control over the temperature of the heat provider. In addition, it has been shown that by changing the geometry of the setup, we were able to create a more homogeneous flow through the sensor chip in comparison to the original setup, as evidenced by the fact that power consumption was also lowered by a factor of two. These improvements have led to an increased effect size and a lower noise level on the measuring signal. These effects, in turn, result in a higher sensitivity of the device in terms of bacterial detection. However, simulations indicate that additional improvement can be made by further adjusting the geometry of the flow cell. The flow cell with its current height and aspect ratio, displays buoyant convection, leading to an asymmetric heat flow through the system. Decreasing the height of the measuring cell and replacing the glass lid on top of the system with a better thermal conductor will further improve the homogeneity of the heat flow, which will have a positive effect on the sensitivity of the device. On the other hand, one should also note that these improvements for thermal sensing are not necessarily beneficial for the multifunctional character of the device in terms of optical observation and impedance spectroscopy. Furthermore, we have developed a two-step calibration algorithm that allows to determine the thermal conductivity of a test liquid, in this case water, with good precision directly from the raw temperature and power data.

Acknowledgements The authors are grateful for funding by the Research Foundation Flanders (FWO) project G0B.6213N "Exploration of heat conductivity effects in bio- and chemo-sensors" and the KULeuven C1 project "Smart Cellular Scaffolds" (C14/15/067). Technical support by Werner Neefs is greatly appreciated.

References

[1] A. P. F. Turner, Chem. Soc. Rev. **42**, 3184–3196 (2013).
[2] B. Van Dorst, J. Metha, K. Bekaert, E. Rouah-Martin, W. De Coen, P. Dubruel, R. Blust, and J. Robbens, Biosens. Bioelectron. **26**, 1178–1194 (2010).
[3] G. Vlatakis, L. I. Andersson, R. Müller, and K. Mosbach, Nature **361**, 645–647 (1993).
[4] K. Yano and I Karube, Trends Anal. Chem. **18**, 199–204 (1999).

[5] K. Haupt and K. Mosbach, Chem. Rev. **100**, 2495–2504 (2000).
[6] H. Shi, W. B. Tsai, M. D. Garrison, S. Ferrar, and B. D. Ratner, Nature **98**, 593–597 (1999).
[7] O. Hayden, K. J. Mann, S. Krassnig, and F. L. Dickert, Angew. Chem. Int. Ed. **45**, 2626–2629 (2006).
[8] K. Eersels, P. Lieberzeit, and P. Wagner, ACS Sens. **1**, 1171–1187 (2016).
[9] R. de la Rica, A. Baldi, C. Fernandez-Sanchez, and H. Matsui, Anal. Chem. **81**, 3830–3835 (2009).
[10] A. Poghossian, M. H. Abouzar, F. Amberger, D. Mayer, Y. Han, S. Ingebrandt, A. Offenhäusser, and M. J. Schöning, Biosens. Bioelectron. **22**, 2100–2107 (2007).
[11] Y. Wang, W. Knoll, and J. Dostalek, Anal. Chem. **84**, 8345–8350 (2012).
[12] T. M. Scholtens, F. Schreuder, S. T. Ligthart, J. F. Swennenhuis, A. G. J. T. Tibbe, J. Greve, and L. W. M. M. Terstappen, Cytometry Part A **79A**, 203–213 (2011).
[13] M. Jenik, R. Schirhagl, C. Schirk, O. Hayden, P. Lieberzeit, D. Plaas, G. Paul, and F. L. Dickert, Anal. Chem. **81**, 5320–5326 (2009).
[14] I. Mannelli, M. Minunni, S. Tombelli, and M. Mascini, Biosens. Bioelectron. **18**, 129–140 (2003).
[15] D. F. Reyes-Romero, O. Behrmann, G. Dame, and G. A. Urban, Sens. Actuators Phys. **13**, 43–51 (2014).
[16] B. van Grinsven, K. Eersels, M. Peeters, P. Losada-Pérez, T. Vandenryt, T. J. Cleij, and P. Wagner, ACS Appl. Mater. Interfaces **6**, 13309–13318 (2014).
[17] B. van Grinsven, N. Vanden Bon, H. Strauven, L. Grieten, M. Murib, K. L. Jiménez-Monroy, S. D. Janssens, K. Haenen, M. J. Schöning, V. Vermeeren, M. Ameloot, L. Michiels, R. Thoelen, W. De Ceuninck, and P. Wagner, ACS Nano **6**, 2712–2721 (2012).
[18] M. Peeters, P. Csipai, A. Weustenraed, B. van Grinsven, R. Thoelen, J. Gruber, W. De Ceuninck, T. J. Cleij, F. J. Troost, and P. Wagner, Anal. Bioanal. Chem. **405**, 6453–6460 (2013).
[19] M. Peeters, B. van Grinsven, T. J. Cleij, K. L. Jiménez-Monroy, P. Cornelis, E. Perez-Ruiz, G. Wackers, R. Thoelen, W. De Ceuninck, J. Lammertyn, and P. Wagner, ACS Appl. Mater. Interfaces **7**, 10316–10323 (2015).
[20] K. Eersels, B. van Grinsven, A. Ethirajan, S. Timmermans, K. L. Jiménez-Monroy, J. Bogie, S. Punniyakoti, T. Vandenryt, J. Hendriks, T. J. Cleij, M. J. A. P. Daemen, V. Somers, W. De Ceuninck, and P. Wagner, ACS Appl. Mater. Interfaces **5**, 7258–7267 (2013).
[21] K. Bers, K. Eersels, B. van Grinsven, M. J. A. F. P. S. Daemen, J. F. J. Bogie, J. J. A. Hendriks, E. Bouwmans, C. Püttmann, C. Stein, S. Barth, G. M. J. Bos, W. T. V. Germeraad, W. De Ceuninck, and P. Wagner, Langmuir **30**, 3631–3639 (2014).
[22] K. Eersels, B. van Grinsven, M. Khorshid, V. Somers, C. Püttmann, C. Stein, H. Diliën, G. M. J. Bos, W. T. V. Germeraad, T. J. Cleij, R. Thoelen, W. De Ceuninck, and P. Wagner, Langmuir **31**, 2043–2050 (2015).
[23] B. van Grinsven, K. Eersels, O. Akkermans, S. Ellermann, A. Kordek, M. Peeters, O. Deschaume, C. Bartic, H. Diliën, E. Steen Redeker, P. Wagner, and T. J. Cleij, ACS Sens. **1**, 1140–1147 (2016).
[24] A. C. Rawstron, F. L. Bennett, S. J. M. O'Connor, M. Kwok, J. A. L. Fenton, M. Plummer, R. de Tute, R. G. Owen, S. J. Richards, A. S. Jack, and P. Hilmen, N. Engl. J. Med. **359**, 575–583 (2008).
[25] M. Cristofanilli, T. G. Budd, M. J. Ellis, A. Stopeck, J. Matera, M. C. Miller, J. M. Reuben, G. V. Doyle, W. J. Allard, L. W. M. M. Terstappen, and D. F. Hayes, N. Engl. J. Med. **351**, 781–791 (2004).
[26] S. Yano, E. Amano, A. Katou, I. Taneda, T. Tsutsui, and T. Murase, J. Food Prot. **77**, 1184–1187 (2014).
[27] U.S. Environmental Protection Agency, Table of Regulated Drinking Water Contaminants (Office of the Federal Register National Archives and Records Administration, Washington, 2010), online.
[28] B. Geerets, M. Peeters, B. van Grinsven, K. Bers, W. De Ceuninck, and P. Wagner, Sensors **13**, 9148–9159 (2013).
[29] R. C. Weast, Handbook of Chemistry and Physics, 48th edition (The Chemical Rubber Co., Cleveland 1967).
[30] Y. S. Touloukian, P. E. Liley, and S. C. Saxena, Thermophysical Properties of Matter − The TPRC Data Series. Volume 3. Thermal Conductivity − Nonmetallic Liquids and Gases (IFI/Plenum, New York 1970).
[31] E. R. Dobrovinskaya, Sapphire: Material, Manufacturing, Applications, 55th edition (Springer Science + Bussiness Media, Dordrecht 2009).